IEEE Access
Multidisciplinary | Rapid Review | Open Access Journal

Received July 28, 2021, accepted August 14, 2021, date of publication August 18, 2021, date of current version August 27, 2021.

Digital Object Identifier 10.1109/ACCESS.2021.3105748

Analytical Airgap Field Model and Experimental Validation of Double Sided Hybrid Excited Linear Flux Switching Machine

NOMAN ULLAH[1,2], (Member, IEEE), FAISAL KHAN[1], (Member, IEEE), ABDUL BASIT[2], WASIQ ULLAH[1], (Graduate Student Member, IEEE), AND IMRAN HASEEB[3]

[1]Department of Electrical and Computer Engineering, COMSATS University Islamabad (Abbottabad Campus), Abbottabad 22060, Pakistan
[2]Pakistan Center for Advanced Studies in Energy, University of Engineering and Technology, Peshawar, Peshawar 25120, Pakistan
[3]Department of Electrical Engineering, Qurtuba University of Science and Information Technology, Dera Ismail Khan 29050, Pakistan

Corresponding author: Noman Ullah (nomanullah@cuiatd.edu.pk)

This work was supported by the Technology Development Fund-Higher Education Commission, Pakistan, under Grant HEC-TDF 03-067.

ABSTRACT Linear Flux Switching Machines (LFSMs) are suitable candidates for long stroke applications as they confines all excitation sources to primary thus leaving completely passive, robust, and low cost secondary. Permanent Magnet LFSMs (PMLFSMs) enables high thrust force density and efficiency. However, deficiency of controllable air-gap flux, risk of PM demagnetization, and increasing cost of rare earth PM materials diverted researchers towards Field Excited LFSMs (FELFSMs). FELFSMs wiped out aforementioned PMLFSM's shortcomings at the cost of low thrust force density. In this paper, merits of PMLFSM and FELFSM are combined by proposing a novel Hybrid Excited LFSM (HELFSM). Proposed machine is excited by PMs, Field Excitation Coils (FECs), and Armature Windings (AWs). However, complex magnetic circuit of poly-excited HELFSM compels designers to adopt FE Analysis (FEA) for design, analysis, and optimization. To decrease dependency on computationally complex and time consuming FEA, an analytical model combining lumped parameter magnetic equivalent circuit, Fourier analysis, Laplace equation, and Maxwell Stress Tensor method is proposed to predict open-circuit flux linkage, B-EMF, normal and tangential components of no-load and on-load magnetic flux density, detent, and thrust force performance. Finally, predictions of the developed analytical model are validated with corresponding FEA and experimental results.

INDEX TERMS Analytical modeling, finite element analysis, hybrid excited linear flux switching machine, lumped parameter magnetic equivalent circuits, maxwell stress tensor, segmented secondary.

I. INTRODUCTION

Safe, reliable, and economical transportation system is the key factor for development of a country. Considering increased carbon emissions and global warming, Internal Combustion Engines (ICEs) were replaced by environment friendly rotatory electrical machines to decrease dependency on decaying fossil fuels and reduce green-house effect [1], [2]. Existing long stroke applications using rotatory machines plus meshing engagement of Mechanical Conversion System (MCS) results in less reliability and efficiency of overall traction system [3], [4]. As linear machines possess a unique ability of producing direct thrust force, faults and less mechanical power transfer problems associated with MCS can be eliminated. Besides these, promising features of high-power density, force density, and efficiency makes linear machines a strong candidate for linear direct-drive applications [5]–[7]. Linear machines can be obtained by splitting longitudinally and unrolling corresponding rotatory machines. However, resultant single sided linear motor was unable to maintain its peak position in application industry due to complementary high normal or attraction forces [8]. These inherent undesired forces exert additional frictional force on the linear bearings, hence reducing output thrust force and reliability of the setup [9]. Unidirectional high normal force demerit of single sided linear machine can

The associate editor coordinating the review of this manuscript and approving it for publication was Paolo Giangrande.

be curtailed by adopting double-sided designs that shows bi-directional normal force waveform and results in an average value of almost zero [10].

Numerous topologies of linear machines such as linear permanent magnet synchronous machine (LPMSM), linear induction machine (LIM), linear switched reluctance machine (LSRM), and linear direct current machine (LDCM) were investigated for direct-drive electric train applications. Technical problems such as high fabrication cost of long stroke LPMSM [6], reduced air-gap average flux linkage and thrust force, stator bars' faults, complex construction and control algorithms in case of LIM [11]–[13], high thrust force ripples resulting in vibrations and acoustic noise, and lower power density problem associated with LSRM [14], [15], and low speed-force gradient and high maintenance cost of LDCM compelled scientists and researchers to explore new topologies.

Linear Flux Switching Machine (LFSM) is a sub-class of Linear Synchronous Machine (LSM) with confinement of all excitation sources to one part of the machine i.e., stator or mover [16]. LFSMs can be categorized according to (a) geometric structure, and (b) excitation sources. Based on geometric structure, LFSMs can be divided into (a) single sided, and (b) double sided design [17]. Depending upon the excitation source, LFSMs can be divided into (a) Permanent Magnet LFSMs (PMLFSMs) [9], (b) Field Excited LFSMs (FELFSMs) [18], and (c) Hybrid Excited LFSMs (HELFSMs) [19]. PMs and Field Excitation Coils (FECs) are main sources of flux in PMLFSM and FELFSM, respectively. PMLFSM reveals drawbacks of uncontrollable air-gap magnetic flux density and risk of PM demagnetization. Furthermore, continuous and rapid increase in rare-earth PM materials prices such as Neodymium, Dysprosium, and Terbium increased manufacturing cost of PMLFSM [20]. Alternatively, DC electromagnets can be utilized to replace PMs and aforementioned PMLFSM's drawbacks can be curtailed with an additional advantage of flux strengthening/weakening capability. However, output thrust force density of FELFSM is low and only few percent to that of PMLFSM. HELFSM is totally a new dimension combining advantages of both PMLFSM and FELFSM by utilizing PMs, FECs, and Armature Windings (AWs) as excitation sources. However, literature regarding HELFSM [20] is very scarce and requires serious attention.

Electromagnetic modelling techniques adopted for design and analysis of hybrid excited machines can be categorized as; (a) Numerical Methods, and (b) Analytical Methods. Due to high accuracy of numerical techniques and complex magnetic flux density waveforms of HELFSMs, FEA is universally utilized for analysis, modelling, and optimization. However, FEA is time consuming and computationally complex specifically when used for initial sizing of the machine [21]. Moreover, FEA consider geometric details and non-linear behaviour of PMs, requiring expensive software/hardware, large computational time, and large drive memory due to repeated iteration [22]. To decrease dependency on FEA, cope with computational complexity, computational time [23], computer memory and drive storage, alternate modelling approaches are developed for design of LFSM. Despite of reduction in computational time, analytical methods have high accuracy with discrepancy less than 5.0% [24]. Analytical models derived from Maxwell equations allow fast exploration of the prototypes in initial design stages, and FEA is performed for refinement of chosen prototype [25].

Literature about analytical techniques developed for LFSM is very limited [26]–[28], and require immediate attention to enhance pre-design predictions. Authors of [26] combined response surface methodology with FEA to calculate influence of design parameters on the LFSM net thrust force. Hybrid analytical approach based on strong coupling of MEC and formal solution of Maxwell's equations for LFSM to predict Magnetic Flux Density (MFD), cogging force, and electromotive force is developed in [27]. Authors of [28] preferred nonlinear MEC for initial design of LFSM due to convenience and swiftness of developed technique and investigated B-EMF, cogging force, and thrust force. A very rare research is reported in the literature regarding analytical modelling for electromagnetic performance prediction of Field Excited FSM. All the aforementioned research mainly focuses on PMFSMs, analytical modelling for electromagnetic performance prediction of HELFSM is essential need of present time and also require serious attention.

In the current technologically developed period, humans and goods delivery suspension down time is not acceptable. Electric train is an environment friendly green solution that can be used for light and heavy load transportations and for in-city transport as well as over long distances. In this paper, a novel double sided HELFSM having segmented secondary, unequal primary tooth width, and complementary coil design forming combination of series/parallel magnetic circuit is proposed for long-stroke linear motion applications. Segmented secondary design provides low reluctance short paths for flux linkage and also reduce material consumption. Unequal primary tooth width, complementary coil design, and combination of series/parallel magnetic circuit enables more symmetrical and sinusoidal flux linkages, resulting in a reduced Thrust Force Ripple Ratio (TFRR). Comparison of existing and proposed traction scheme for electric train is shown in Figure 1. Proposed configuration have the ability to; wipe out meshing engagement of rotatory machines and MCS, diminish high normal force problem of single sided design, reflect high thrust force density of PM excited machines, and air-gap field strengthening/weakening due to hybrid excitation.

Rest of the paper is organized as following. Design topology, complementary coil design guidelines, geometry design variables, and working principle of HELFSM is explained in Section II. Two dimensional analytical model based on lumped parameter magnetic equivalent circuit, Fourier analysis, Laplace equation, and Maxwell Stress Tensor method is proposed in Section III. Analytical model predictions for

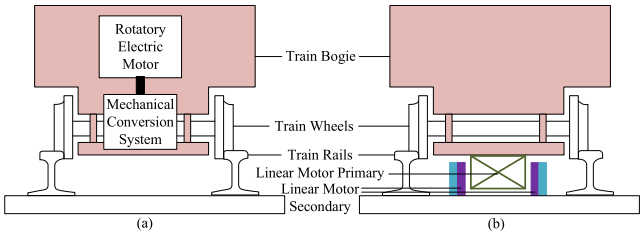

FIGURE 1. Electric traction system, (a) existing scheme, (b) proposed electric train powered by double sided hybrid excited linear flux switching machine.

open-circuit flux linkage, B-EMF, normal and tangential components of no-load and on-load magnetic flux density, detent, and thrust force are validated with corresponding FE Analysis results in Section IV. Proposed machine is quantitatively compared state-of-the-art HELFSM design of literature [20] in Section V. Experimental test bed and validation of analytical predications with corresponding measured results is presented in Section VI. Finally, some conclusions are drawn in Section VII.

II. TOPOLOGY AND WORKING PRINCIPLE

A. TOPOLOGY OF PROPOSED HELFSM

3-D illustration and corresponding 2-D schematic diagram of proposed HELFSM is shown in Figure 2 and Figure 3, respectively. Number of primary teeth (P_t), PM or DC windings ($W_{PM/DC}$), AC windings (W_{AC}), and stator to mover pole pitch ($\tau s/\tau m$) of the proposed complementary coil design HELFSM having combination of series/parallel magnetic circuit is achieved utilizing following design guidelines equations:

$$P_t = 4ab + 1 \tag{1}$$

$$W_{PM/DC} = 2ab + 1 \tag{2}$$

$$W_{AC} = 2ab + 1 \tag{3}$$

$$\tau_s/\tau_m = 4ab/(2ab + 2) \tag{4}$$

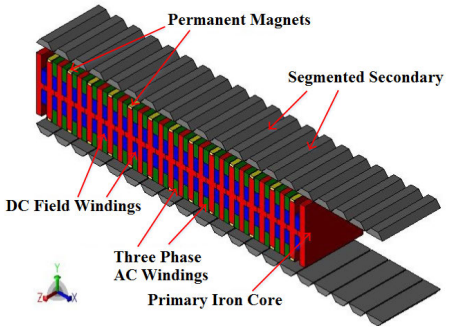

FIGURE 2. 3-D structure of proposed HELFSM.

where, $a = 3$ and is quantity of AC phases and $b = 2$ that indicates AC winding coil pair repetition. Aforementioned equations lead to single side guidelines of $P_t = 25$, $W_{PM/DC} = 13$, $W_{AC} = 12$, and $\tau s/\tau m = 24/14$. Structure design variables are presented in Figure 4 and their values are tabulated in Table 1.

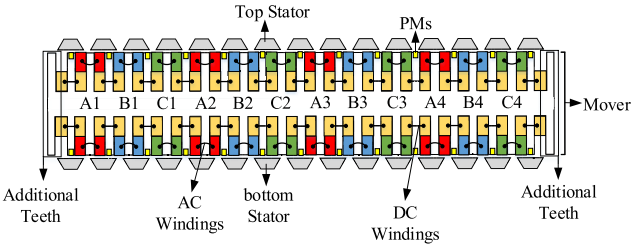

FIGURE 3. 2-D schematic diagram of proposed HELFSM.

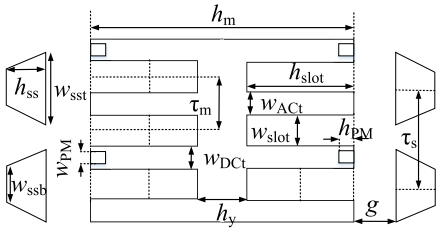

FIGURE 4. Design variables.

TABLE 1. Structure design parameters.

Symbol	Parameter(Unit)	Value
τ_m	Mover pole pitch (mm)	35
τ_s	Stator pole pitch (mm)	30
h_m	Mover height (mm)	91
$h_s = 2 * h_{ss}$	Stator height (mm)	19
w_{DCt}	Mover DC tooth width (mm)	9.5
w_{ACt}	Mover AC tooth width (mm)	8.5
w_{slot}	Slot width (mm)	8.5
h_{slot}	Slot height (mm)	20.6
h_y	Mover yoke height (mm)	8.6
w_{PM}	PM width (mm)	7
h_{PM}	PM height (mm)	3.5
V_{PM}	PM volume (mm^3)	6500
w_{sst}	Stator segment tip width (mm)	28.5
w_{ssb}	Stator segment base width (mm)	12.825
h_{ss}	Stator segment height (mm)	9.5
g	Air-gap height (mm)	2
L	Stack length (mm)	10
v	Mover velocity (m/s)	1.5
$N_{AC\&DC}$	Number of AC and DC coil turns	40
J_{AC}	AC current density (A/mm^2)	4.57
J_{DC}	DC current density (A/mm^2)	4.52

B. WORKING PRINCIPLE OF PROPOSED HELFSM

Working principle of proposed HELFSM can either be explained with the help of air-gap field modulation theory [29] or through magnetic circuit. Later one methodology is adopted in this paper to reduce complexity. Linear displacement of one stator pole pitch representing 360 electrical degrees with two important points of positive maximum flux linkage and negative maximum flux linkage is shown in Figure 5. Red lines indicate flux flow generated due to PMs and makes series magnetic circuit encompassing two stators and complete mover. Flux represented by green lines is due to DC electromagnets and make combination of two parallel magnetic circuits and also follow PM flux flow paths. Positive maximum flux linkage of Phase A is shown in Figure 5(a)

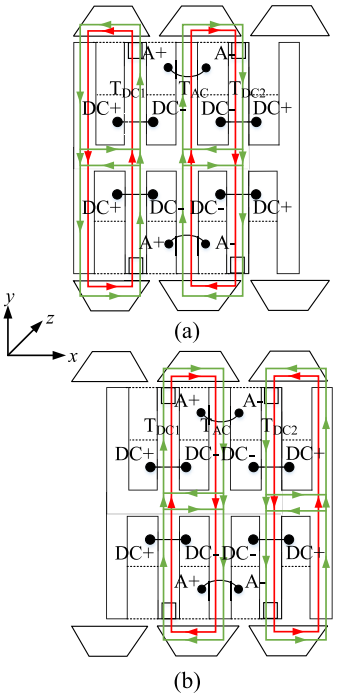

FIGURE 5. Magnetic circuit based working principle, (a) positive maximum flux linkage, and (b) negative maximum flux linkage.

and negative maximum flux linkage is shown in Figure 5(b). Both PM and DC electromagnets' flux follow same paths to ensure philosophy of hybrid excitation, bipolar sinusoidal flux linkage, and flux strengthening/weakening phenomenon.

III. ANALYTICAL MODEL FOR ELECTROMAGNETIC PERFORMANCE OF HELFSM

Electromagnetic performance of HELFSM is predicted utilizing Lumped Parameter Magnetic Equivalent Circuit (LPMEC) for prediction of open-circuit flux linkage and B-EMF, Laplace Equations (LEs) in term of vector potential for prediction of Magnetic Flux Density (MFD), Maxwell Stress Tensor (MST) method in the mid of air-gap for prediction of no-load detent force, and thrust force. Mathematical expressions and assumptions of utilized analytical techniques are discussed as following;

A. LPMEC

This section introduces general analytical equations utilized for solving node magnetic potentials employing incidence matrix methodology. Unit section sketch diagram for HELFSM is shown in Figure 6(a) and corresponding LPMEC model is shown in Figure 6(b), encompassing segmented stator, mover, PMs, FECs, and air-gap. As the proposed model is a double-sided topology and both side's geometric structure and excitations are identical, hence only one side of the machine is modelled to reduce computational complexity. Two PM+FEC mover teeth, three AW teeth, and three stator segments are considered to explain the LPMEC. Total of eight structure based nodes denoted as capital roman numbers

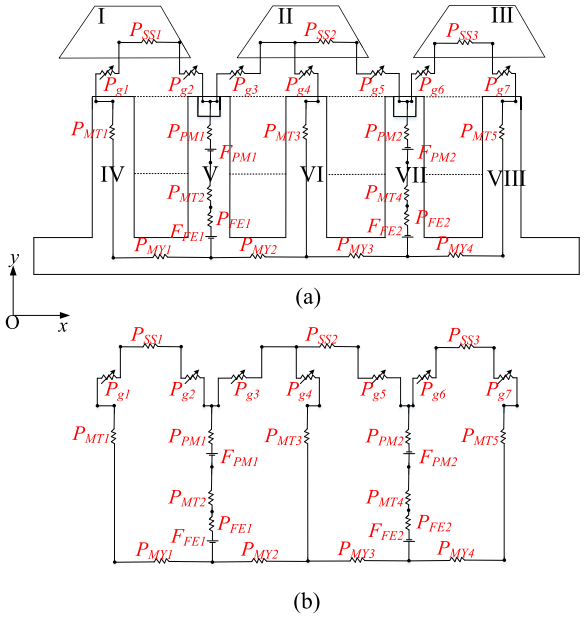

FIGURE 6. Unit section of HELFSM, (a) 2-D schematic diagram, (b) LPMEC.

(shown as I,II...VIII) are declared in the developed LPMEC. Air-gap MEC module is sensitive to mover position. Whereas stator, mover, FEC, and PM MEC modules are considered as invariant. In this section, air-gap MEC module for HELFSM is modelled for five different mover to stator positions, under following assumptions.

- Ferromagnetic core has infinite permeability
- End effects are neglected, and
- Magnetic saturation is not accounted.

1) PM, MOVER, AND STATOR MEC

Permeances of stator segment (denoted as $\mathcal{P}_{SSi}$), mover teeth (defined as $\mathcal{P}_{MTi}$), mover yoke (depicted as $\mathcal{P}_{MYi}$) included in the LPMEC are calculated utilizing Equation 5, 6, and 7, respectively. PM is modelled as magnetomotive force source with permeance in series, hence Equation 8 and 9 are utilized to calculate F_{PM} and $\mathcal{P}_{PM}$. Similarly, due to hybrid excitation magnetomotive force of FECs is also accounted and Equation 10 is utilized to calculate F_{FEC}.

$$\mathcal{P}_{SSi} = \frac{\mu_0 \mu_r w_{ssti} L}{h_{ssi}} \tag{5}$$

$$\mathcal{P}_{MTi} = \frac{\mu_0 \mu_r w_{mti} L}{h_{mti}} \tag{6}$$

$$\mathcal{P}_{MYi} = \frac{\mu_0 \mu_r w_{myi} L}{h_{myi}} \tag{7}$$

$$\mathcal{F}_{PM} = \frac{B_r w_{PM}}{\mu_0 \mu_r} \tag{8}$$

$$\mathcal{P}_{PM} = \frac{\mu_0 \mu_r A_{PM}}{L} \tag{9}$$

$$\mathcal{F}_{FEC} = N * I \tag{10}$$

where, i is a positive integer and represent stator segment, mover tooth, and mover yoke number, μ_0 is permeability

of free space, μ_r is PM relative permeability, A_{PM} is PM area, N is number of FEC turns, and I is the current supplied to FECs.

2) AIR-GAP MEC

Distribution of magnetic flux within the air-gap varies as a function of stator segment position with respect to mover. Multiple air-gap MEC modules are developed corresponding to various stator versus mover positions. Five different air-gap MEC modules are developed, when one mover pole pitch covers linear displacement of one stator pole pitch. Due to periodic nature of HELFSM only five air-gap MEC modules are required for validation of open-circuit flux linkage. Flux linkage through air-gap and between mover and stator follows specific paths known as flux tubes. Three types of flux tubes are observed during FE Analysis of HELFSM having perpendicular flux flow directions (cross sections are shown in Figure 7), hence Equation 11, 12, and 13 are utilized to compute its permeances.

$$\mathcal{P}_{g(a)j} = \frac{\mu_0 L \ln\left(\frac{r_2}{r_1}\right)}{\theta} \tag{11}$$

$$\mathcal{P}_{g(b)j} = \frac{\mu_0 L x}{h} \tag{12}$$

$$\mathcal{P}_{g(c)j} = \frac{2\mu_0 L \ln\left(1 + \frac{\pi x}{\pi r + 2h}\right)}{\pi} \tag{13}$$

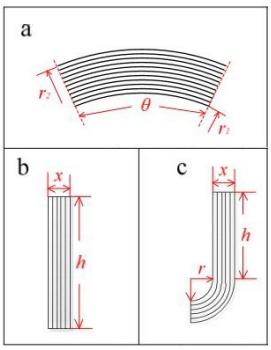

FIGURE 7. Cross sections of air-gap flux tubes.

where, j is a positive integer and represent number of air-gap flux tubes, r_1 represent inner radius, r_1 represent outer radius, θ shows tangential length of the flux tube, x and h is width and height of b and c-type flux tube, and r is the inner radius of curvature present at the end of c-type flux tube. Mover, stator, and air-gap MEC modules at five different stator versus mover positions are described in the form of matrices; these matrices are merged and solved using incidence matrix method utilizing MATLAB Software. Incidence matrix A of a circuit having k structure based nodes and l air-gap branches is kxl matrix, as presented in Equation 14.

$$A_{k,l} = \begin{cases} 0, & \text{when branch } l \text{ is not connected to node } k, \\ -1, & \text{when branch } l \text{ ends to node } k, \\ 1, & \text{when branch } l \text{ begins from node } k. \end{cases} \tag{14}$$

Air-gap flux tubes obtained from FE Analysis for five different stator versus mover positions (termed as Position 1 to Position 5) are shown in Figure 8. MEC modules, flux flow paths and corresponding directions for Position 1 to 5 are shown in Figure 9-13. Both 2-D schematic diagram and LPMEC for Position 1 are shown in Figure 9, whereas only LPMEC for the rest of four positions are presented in Figure. 10-13. Air-gap permeances of figures are denoted in the form of $\mathcal{P}(m, n)$, where m represent mover versus stator position number and n represents sequential flux tube number. Parallel air-gap permeances observed in figures are

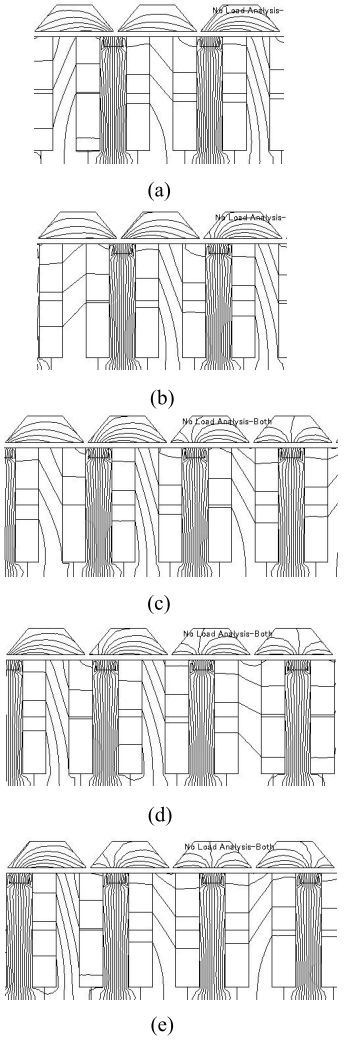

FIGURE 8. Flux tubes obtained from FE analysis at five different mover versus stator positions; (a) Position 1, (b) Position 2, (c) Position 3, (d) Position 4, (e) Position 5.

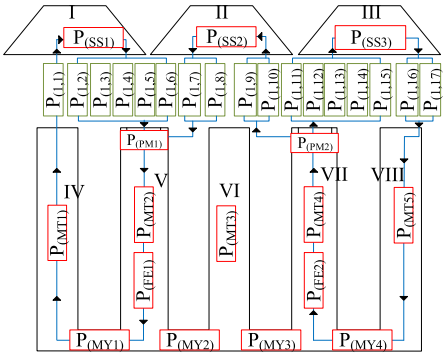

(a)

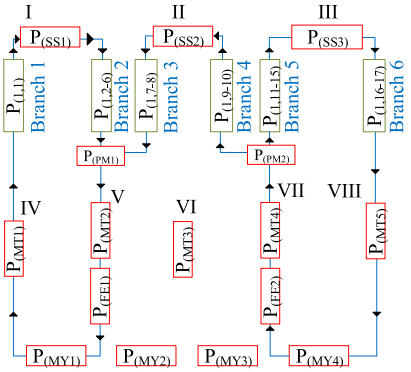

(b)

FIGURE 9. Position 1 LPMEC; (a) 2-D schematic diagram, (b) LPMEC.

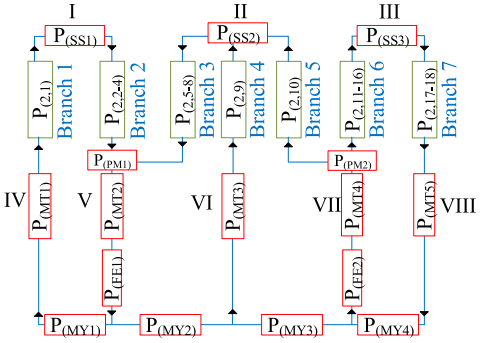

FIGURE 10. Position 2 LPMEC.

combined according to standard circuit analysis guidelines and are presented as single branch in corresponding LPMEC.

Magnetic potential of each node can be derived by applying Kirchhoff Circuit Law

$$U = A^t.V \tag{15}$$

where, U is the magnetomotive force drop across each branch and is $n \times 1$ vector, A is incidence matrix of $m \times n$ dimensions, and V is magnetic potential on each node ($m \times 1$ vector).

Product of incidence matrix A and flux Φ ($n \times 1$ vector) through each branch is equal to zero and can be represented as Equation 16

$$\mathrm{A}.\,\Phi = 0 \tag{16}$$

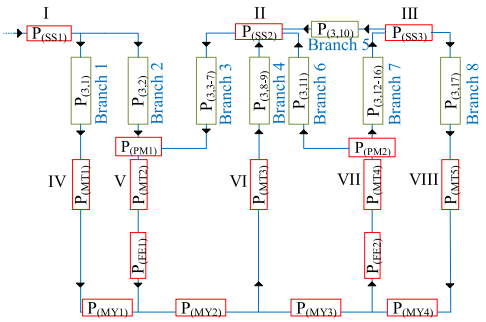

FIGURE 11. Position 3 LPMEC.

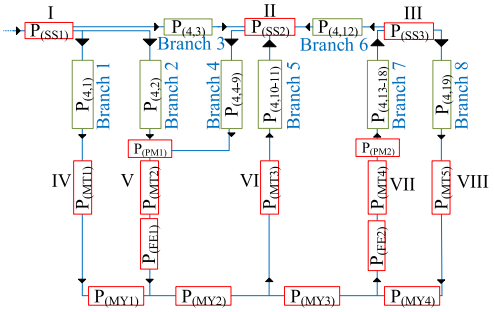

FIGURE 12. Position 4 LPMEC.

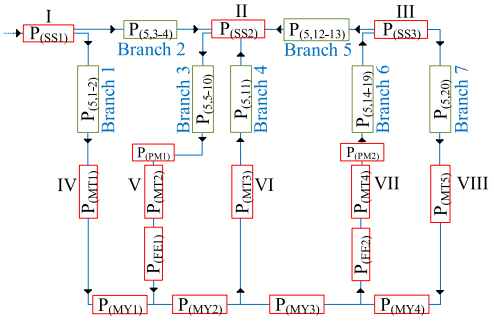

FIGURE 13. Position 5 LPMEC.

Equation 15 and Equation 16 can be merged to generate Equation 17

$$U = \mathcal{R}.\Phi + E = \Lambda^t.\Phi + E \tag{17}$$

where, $\mathcal{R}$ is $n \times n$ diagonal matrix representing reluctance of each branch, E is magnetomotive force source in each branch ($n \times 1$ vector), and Λ is $n \times n$ diagonal matrix representing permeance of each branch.

Equation 18 is the formula derived by using A, Λ, and E are utilized for calculation of magnetic potential

$$V = \left(A.\Lambda.A^t\right)^{-1} \cdot (A.\Lambda.E) \tag{18}$$

The phase B-EMF is determined by utilizing no-load flux linkage obtained from LPMEC and Equation 19.

$$EMF = -N_{AC}\frac{d\psi_m}{dt} = -N_{AC}\frac{\Delta\psi_m}{\Delta x}.v \tag{19}$$

B. FOURIER SERIES IN CONJUNCTION WITH LAPLACE EQUATION

Cartesian coordinated reference system $x - y$ is utilized to determine MFD components in the mid of air-gap. In this section, slotting effects are considered by introducing carter coefficient [30]. Normal and tangential components of MFD under no-load and on-load condition are analytically determined by solving Laplace Equation [31] in term of vector potential.

No-load and on-load average MFD originate at the mid of air-gap i.e., $y = g/2$, and can be illustrated as Equation 20,

$$B_{avg}\tau_m = \int_{-\frac{\tau_m}{2}}^{\frac{\tau_m}{2}} B_y(x, g/2)\, dx \tag{20}$$

where, B_{avg} is average magnetic flux density, B_y is MFD component, and g is the air-gap height. Since MFD is symmetric about the origin, this leads to boundary condition along xy and $x'y'$ as illustrated in Figure 14 and Equation 21,

$$B_x\,(\tau_m/2, y) = B_x\,(-\tau_m/2, y) = 0 \quad \forall y \epsilon [0, g] \tag{21}$$

Due to assumption of iron core infinite permeability, MFD along xx' and yy' boundaries of x-axis and y-axis respectively modifies boundary condition as shown in Figure 14 and Equation 22,

$$B_x(x, 0) = 0 \quad \forall x \in [-\tau_m/2, \tau_m/2] \tag{22}$$

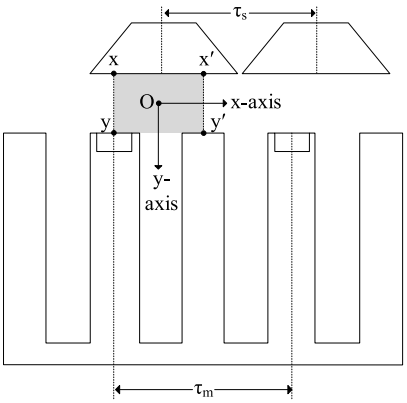

FIGURE 14. Boundary conditions.

The constant average MFD fulfilling boundary condition over the interval $x \in [-\tau_m/2, \tau_m/2]$ is presented as Equation 23,

$$B_{avg} = \frac{1}{\tau_m}\int_{-\frac{\tau_m}{2}}^{\frac{\tau_m}{2}} B_y(x, y)dx \tag{23}$$

Substituting aforementioned mathematical assumptions, results in B_x component of MFD (section between mover tooth and mid of air-gap) in the form of Fourier series as Equation 24,

$$B_{\text{lower part}}\,(x) = \sum_{n=1}^{\infty} F_n \sin\left(\frac{2\pi nx}{\tau_m}\right) \tag{24}$$

Fourier series coefficient is shown in Equation 25,

$$F_n = \frac{4.C \cdot W_n}{\tau_m} \tag{25}$$

The constant term W_n for any positive integer can be evaluated by numerical solution of integral as shown in Equation 26,

$$W_n = \int_0^{w_{slot}} \left[\frac{1}{\sqrt[3]{\frac{w_{slot}}{2} - x}} - \frac{1}{\sqrt[3]{\frac{w_{slot}}{2} + x}}\right] \sin\left(\frac{2\pi nx}{\tau_m}\right) \tag{26}$$

The constant parameters C is obtained from Carter coefficient, defined as ratio of maximum MFD (in the mid of air-gap) to average MFD given by Equation 27,

$$k_c = \frac{B_{\max}}{B_{avg}} \tag{27}$$

where,

$$B_{\max} = B_{avg} - \sum_{n=1}^{\infty} \frac{2\pi nA_n \cos(\pi n)}{\tau_m} \cosh\left(\frac{\pi ng}{\tau_m}\right) \tag{28}$$

$$B_{\max} = B_{avg} - \sum_{n=1}^{\infty} (-1)^n \frac{4CW_n \cosh\left(\frac{\pi ng}{\tau_m}\right)}{\tau_m \sinh\left(\frac{2\pi ng}{\tau_m}\right)} \tag{29}$$

$$B_{\max} = B_{\text{avg}} - \sum_{n=1}^{\infty} \frac{2(-1)^n CW_n}{\tau_m \sinh\left(\frac{\pi ng}{\tau_m}\right)} \tag{30}$$

Substituting Equation 30 in Equation 27, the constant parameter C as a function of B_{avg} can be obtained and written as Equation 31,

$$C = \frac{(k_c - 1)\, B_{avg}}{K} \tag{31}$$

The parameter K in Equation 31 can be written as Equation 32,

$$K = -\sum_{n=1}^{\infty} \frac{2(-1)^n W_n}{\tau_m \sinh\left(\frac{\pi ng}{\tau_m}\right)} \tag{32}$$

Substituting Equation 32 in Equation 31, the constant parameter C can be modified as Equation 33,

$$C = \frac{(k_c - 1)\, B_{avg}}{-\sum_{n=1}^{\infty} \frac{2(-1)^n W_n}{\tau_m \sinh\left(\frac{\pi ng}{\tau_m}\right)}} \tag{33}$$

Final analytical expression of MFD is obtained by vector potential governed by general form of LE as shown in Equation 34.

$$\frac{\partial^2 P}{\partial x^2} + \frac{\partial^2 P}{\partial y^2} = 0 \tag{34}$$

Solving for vector potential and its relevant boundary condition, MFD can be express as Equation 35,

$$B_x(x, y) = \frac{\partial P(x, y)}{\partial y} \text{ and } B_y(x, y) = -\frac{\partial P(x, y)}{\partial x} \tag{35}$$

Conveniently, General LE of Equation 34 can be written as Equation 36,

$$P(x,y) = -B_{\text{avg}}\, x + \sum_{n=1}^{\infty} A_n \cosh\left(\frac{2\pi ny}{\tau_m}\right) \sin\left(\frac{2\pi nx}{\tau_m}\right) \quad (36)$$

The constant term A_n can be computed by utilizing Equation 37,

$$A_n = \frac{2CW_n}{n\pi \sinh\left(\frac{2\pi gn}{\tau_m}\right)} \quad (37)$$

Based on Equation 35, MFD components from Equation 36 becomes as Equation 38 and Equation 39,

$$B_x(x,y) = \sum_{n=1}^{\infty} \frac{2n\pi A_n}{\tau_m} \sinh\left(\frac{2n\pi y}{\tau_m}\right) \sin\left(\frac{2n\pi x}{\tau_m}\right) \quad (38)$$

$$B_y(x,y) = \sum_{n=1}^{\infty} \frac{2n\pi A_n}{\tau_m} \cosh\left(\frac{2n\pi y}{\tau_m}\right) \cos\left(\frac{2n\pi x}{\tau_m}\right) \quad (39)$$

Incorporating boundary conditions of Equation 21 and Equation 22, and by substituting constant term A_n defined in Equation 37, MFD of Equation 38 and Equation 39 can be rewritten as Equation 40 and Equation 41,

$$B_x(x,y) = \sum_{n=1}^{\infty} \frac{4CW_n \sinh\left(\frac{2n\pi y}{\tau_m}\right) \sin\left(\frac{2n\pi x}{\tau_m}\right)}{\tau_m \sinh\left(\frac{2n\pi g}{\tau_m}\right)} \quad (40)$$

$$B_y(x,y) = \sum_{n=1}^{\infty} \frac{4CW_n \cosh\left(\frac{2n\pi y}{\tau_m}\right) \cos\left(\frac{2n\pi x}{\tau_m}\right)}{\tau_m \sinh\left(\frac{2n\pi g}{\tau_m}\right)} \quad (41)$$

Equation 40 and Equation 41 are used for calculation of MFD components.

C. MAXWELL STRESS TENSOR (MST) METHOD

One of the major reason of high TFRR is detent force. Detent force is due to slotting effect (having wavelength of one mover pole pitch) and end force (having wavelength of one stator pole pitch). Utilizing open-circuit normal and tangential components of MFD (calculated by using Equation 40 and Equation 41), detent force can be predicted by mean of MST method, and can be expressed as Equation 42,

$$F_{\text{Detent}} = \frac{GCD\,(N_{ms}, N_{ss})\,.L}{\mu_o} \int_0^{L_{perp}} B_x(x,y).B_y(x,y).d\,x \quad (42)$$

where, N_{ms} represents number of mover slots, N_{ms} depicts number of stator segments, and L_{perp} is the perpendicular x-direction length of the mover.

Thrust force of proposed HELFSM for one mover pole pitch is predicted by solving MST Equation 43. It is important to mention that on-load normal and tangential components of MFD components are utilized for thrust force predication.

$$F_{\text{Thrust}} = \frac{L}{\mu_o} \sum_{n=-\infty}^{\infty} \int_o^{\tau_m} \left(B_x(x,y) \cdot B_y(x,y)\right) dx \quad (43)$$

IV. FE ANALYSIS VALIDATIONS

Predictions of developed 2-D analytical model are validated with universally accepted FEA results utilizing JMAG Commercial FEA Package ver. 18.1. Comparison of predicted and FEA results for no-load flux linkage, B-EMF, normal and tangential components of no-load MFD, detent, and thrust force profile is presented in Figure 15-19, respectively. In order to increase ease of understanding, only center phase (C-Phase) flux linkage and B-EMF is discussed. All results presented in this section are under hybrid excitation (i.e., PM+FEC).

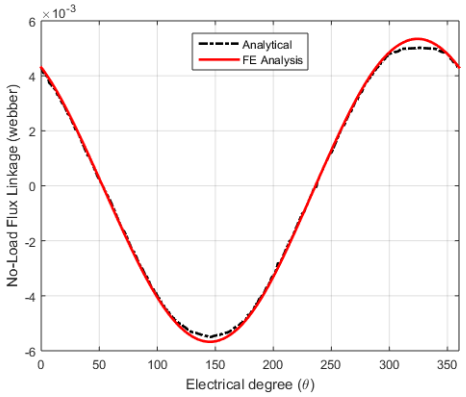

FIGURE 15. Comparison of no-load flux linkage predicted by analytical model and FEA.

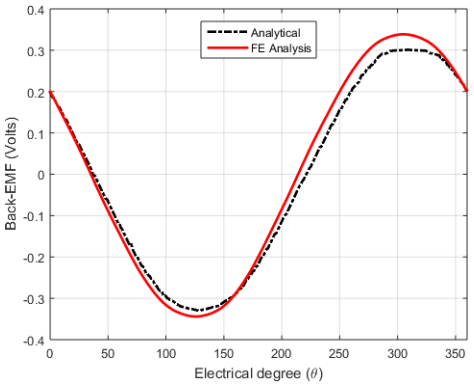

FIGURE 16. Comparison of B-EMF predicted by analytical model and FEA.

It can be seen that analytical predictions for all Key Performance Indicators (KPIs) shows good agreement with that of FEA results. While comparing analytical predictions and FEA results, maximum percentage error of 4.9% is recorded for no-load flux linkage, 4.6% for B-EMF, 2.3% for MFD components, 3.8% for detent force, and 3.3% for thrust force profile. As the B-EMF waveform is obtained by direct multiplication of predicted no-load flux linkage, number of AC turns per coil, and velocity of the mover. A little phase shift can be observed in the B-EMF plot. Reason behind x-direction phase shift is calculation methodology and magnetic circuit of proposed machine. MFD waveforms are repetitive in nature and are densely populated plots, hence a small

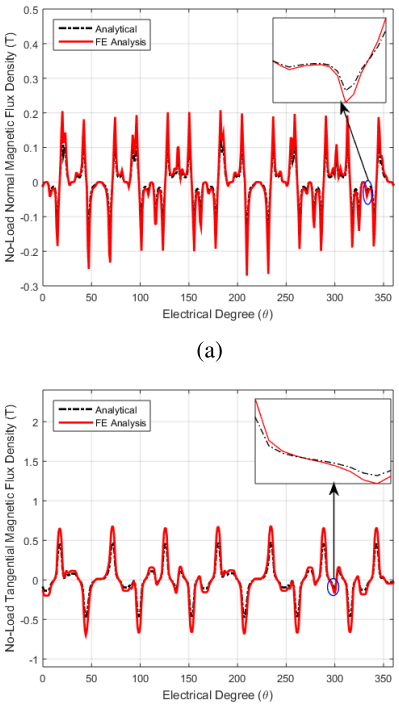

FIGURE 17. Comparison of no-load MFD predicted by analytical model and FEA; (a) Normal component, (b) Tangential component.

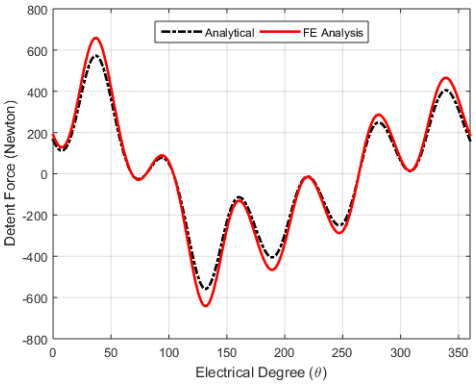

FIGURE 18. Comparison of detent force predicted by analytical model and FEA.

zoom box is utilized to differentiate output of both analysis techniques. Results of analytical predictions for both normal and tangential components of no-load MFD agrees well with these of FEA outputs.

Accuracy of the analytical model for open circuit flux linkage and B-EMF depends upon number of structural nodes defined in the LPMEC and number of output values counted during one electrical cycle. Whereas accuracy of the analytical model for detent, and thrust force depends upon accuracy of LEs solution utilized for MFD prediction. As no-load MFD components with combination of MST method are utilized for solution of detent force predictions. Similarly, on-load MFD components are involved in the on-load

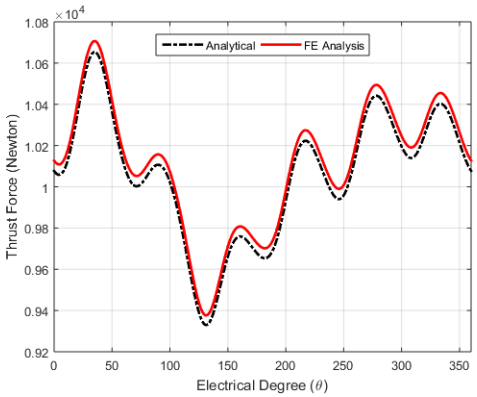

FIGURE 19. Comparison of thrust force predicted by analytical model and FEA.

KPI (thrust force). Good agreement of analytical and FEA results can also be witnessed in all the forces' performance of proposed machine.

Significant reduction in the solution time is observed while comparing FEA and proposed analytical model. Computational time for FEA simulation is almost 24 hours using Core i5 8th generation with 16GB RAM. Triangular mesh having size of 2mm is utilized to simulate proposed machine. Developed mesh resulted in 12918 number of nodes and 23578 number of elements. Whereas proposed analytical model provides a little less accurate results for the same simulation in fraction of a minute.

V. COMPARISON OF PROPOSED AND STATE-OF-THE-ART HELFSM

Proposed machine is quantitatively compared with the only available double-sided HELFSM [20] in literature. Design dimensions, electrical loading, PM volume, velocity, and stack length of the proposed design are made identical with the literature design for fair comparison and is simulated utilizing same JMAG Commercial FEA Package. Nephogram of magnetic flux density obtained from FEA for proposed and state-of-the-art literature HELFSM design is shown in Figure 20. Three phase no-load flux linkage, detent force, and thrust force profile of proposed and literature design

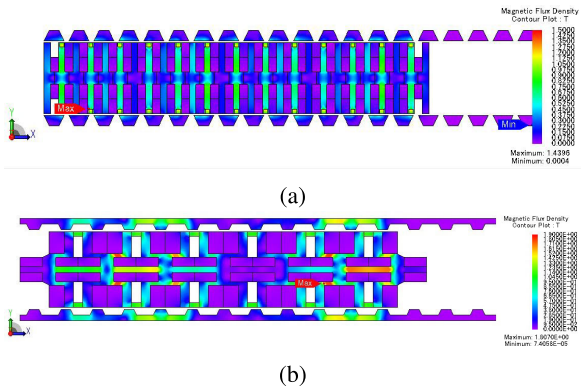

FIGURE 20. Magnetic flux density nephogram; (a) Proposed design, (b) Literature design.

under hybrid excitations are compared in Figure 21-23, respectively.

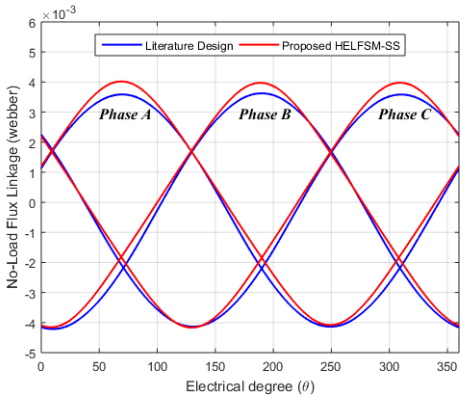

FIGURE 21. Comparison of three phase no-load flux linkage.

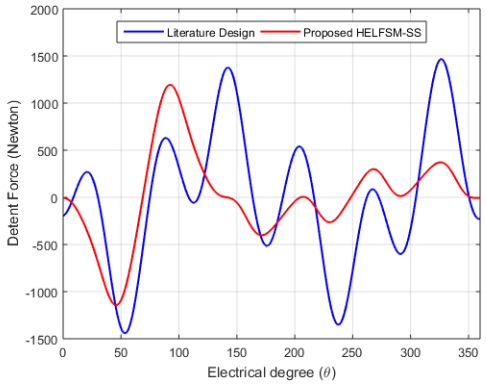

FIGURE 22. Comparison of detent force profile.

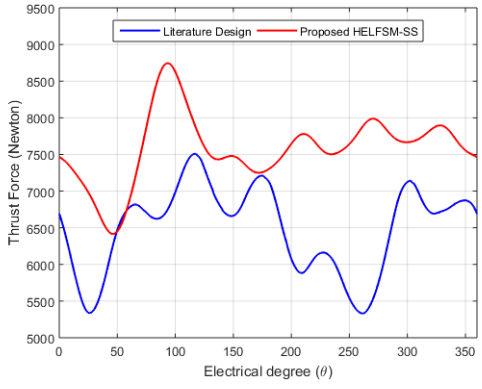

FIGURE 23. Comparison of thrust force profile.

Regarding three phase no-load flux linkage comparison, peak-to-peak value of C-Phase of literature design is 7.72mWb with positive max of 3.58mWb and negative max of 4.14mWb. Whereas that of proposed design is 8.10mWb with positive max of 4.02mWb and negative max of 4.08mWb. THD of C-Phase flux linkage of literature design is 6.54% whereas that of proposed design is 4.76%. In-depth analysis revealed that three phase no-load flux linkage of proposed design is higher in magnitude, more sinusoidal, and more symmetrical along y-axis.

Peak-to-peak value of detent force shown by literature design is 2907.6N whereas that of proposed design is 2338.65N. Also, frequency of to and fro motion in one electrical cycle is double when compared with proposed design, as two major pulls and two pushes are recorded during analysis. These multiple fluctuations result in severe TFRR of the machine. Based on above discussion, detent force performance of proposed machine is better than conventional literature design in terms of magnitude and its fluctuation frequency.

Average thrust force of 6490.27N, with max value of 7509.09N, min value of 5331.89N, and TFRR of 33.54% were noted down during investigation of conventional literature design. Whereas average thrust force and TFRR of proposed design are 7581.32N and 30.71%. Comparison revealed that average thrust force of proposed design is higher in magnitude and contains less fluctuation forces.

VI. EXPERIMENTAL VALIDATIONS

To validate the theoretical analysis, a full-scale prototype of HELFSM is manufactured, detailed structure of mover, stator assembly, measurement setup, and test bed is shown in Figure 24. Stroke length of the prototype motor is 2m. Material for mover core and stator segment is 35H210 and PMs used in the machine is Neomax-35AH having parallel magnetization pattern. SWG 18 conductor is used for winding purpose, measured resistance and inductance of each AC phase is 0.7ohm and 0.99mH, respectively. Whereas, that of DC coil is 2.1ohm and 7.5mH, respectively.

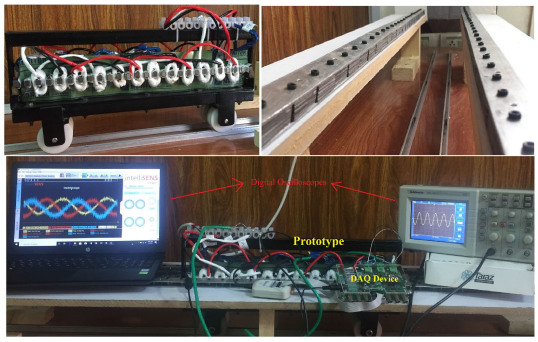

FIGURE 24. HELFSM prototype and test bed.

FE Analysis, analytical, and experimental results of two electromagnetic performance indicators i.e. center phase no-load B-EMF and detent force are presented in Figure 25 and Figure 26. Experimental results are recorded using intelliSENS DAQ device and electrical resistance strain sensor. Under no-load condition, proposed machine was driven by servo motor at the rated speed of 1500mm/s resulting in a B-EMF frequency of 50Hz. It can be seen that the results obtained by experiment show a good agreement with corresponding analytical and FEA. A minor deviation in the

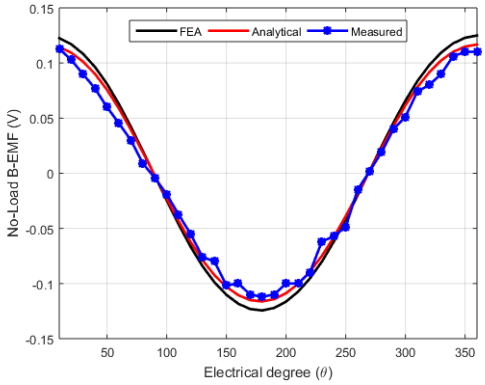

FIGURE 25. No-load induced B-EMF at 1.5m/s.

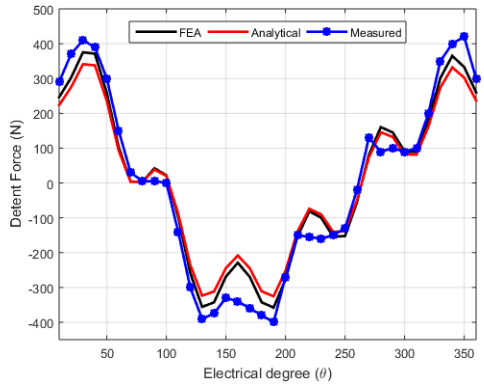

FIGURE 26. Detent force comparison.

results comparison is due to manufacturing imperfection and assembly impreciseness.

VII. CONCLUSION

Hybrid Excited Linear Flux Switching Machines (HELFSMs) are competent candidates for long distance direct drive linear motion applications due to unique features of; (a) controllable air-gap flux density thus enabling flux weakening/strengthening, (b) less rare earth PM volume consumption therefore reducing manufacturing cost, and (c) fault tolerant capability due to redundant excitation sources. HELFSM researched in this paper possess additional advantages of; (1) double-sided design hence solving undesired normal/attraction force problem, (2) segmented secondary thus reducing secondary's material consumption and cost, (3) unequal primary tooth width that enable more symmetrical and sinusoidal flux linkages, (4) and combination of series/parallel magnetic circuit resulting in a reduced thrust force ripple ratio.

To decrease dependence on computationally complex and time consuming FE Analysis, a 2-D analytical model combining LPMEC, Fourier series, LEs, and MST methodology is developed and electromagnetic performance of the proposed machine is predicted. Predicted performance is validated against corresponding FE Analysis and measured results, showing a good agreement. It is proved that the developed analytical model can generate enough accurate results in a fraction of time required for FEA.

REFERENCES

[1] M. Ehsani, Y. Gao, and J. M. Miller, "Hybrid electric vehicles: Architecture and motor drives," *Proc. IEEE*, vol. 95, no. 4, pp. 719–728, Apr. 2007.

[2] N. Arvidsson, J. Woxenius, and C. Lammgård, "Review of road hauliers' measures for increasing transport efficiency and sustainability in urban freight distribution," *Transp. Rev.*, vol. 33, no. 1, pp. 107–127, Jan. 2013.

[3] R. Hellinger and P. Mnich, "Linear motor-powered transportation: History, present status, and future outlook," *Proc. IEEE*, vol. 97, no. 11, pp. 1892–1900, Nov. 2009.

[4] R. Cao, M. Cheng, C. Mi, W. Hua, and W. Zhao, "Comparison of complementary and modular linear flux-switching motors with different mover and stator pole pitch," *IEEE Trans. Magn.*, vol. 49, no. 4, pp. 1493–1504, Apr. 2013.

[5] W. Zhao, M. Cheng, J. Ji, R. Cao, Y. Du, and F. Li, "Design and analysis of a new fault-tolerant linear permanent-magnet motor for maglev transportation applications," *IEEE Trans. Appl. Supercond.*, vol. 22, no. 3, Jun. 2012, Art. no. 5200204.

[6] R. Cao, M. Cheng, C. Mi, W. Hua, X. Wang, and W. Zhao, "Modeling of a complementary and modular linear flux-switching permanent magnet motor for urban rail transit applications," *IEEE Trans. Energy Convers.*, vol. 27, no. 2, pp. 489–497, Jun. 2012.

[7] W. Hao and Y. Wang, "Analysis of double-sided sandwiched linear flux-switching permanent-magnet machines with staggered stator teeth for urban rail transit," *IET Elect. Syst. Transp.*, vol. 8, no. 3, pp. 175–181, Sep. 2018.

[8] F. Xiao, Y. Du, Y. Sun, H. Zhu, W. Zhao, W. Li, T. W. Ching, and C. Qiu, "A novel double-sided flux-switching permanent magnet linear motor," *J. Appl. Phys.*, vol. 117, no. 17, May 2015, Art. no. 17B530.

[9] W. Hao, Y. Wang, and Z. Deng, "Study of two kinds of double-sided yokeless linear flux-switching permanent magnet machines," in *Proc. IEEE Vehicle Power Propuls. Conf. (VPPC)*, Oct. 2016, pp. 1–6.

[10] A. Gandhi and L. Parsa, "Thrust optimization of a flux-switching linear synchronous machine with yokeless translator," *IEEE Trans. Magn.*, vol. 49, no. 4, pp. 1436–1443, Apr. 2013.

[11] T. Higuchi, S. Nonaka, and M. Ando, "On the design of high-efficiency linear induction motors for linear metro," *Electr. Eng. Jpn.*, vol. 137, no. 2, pp. 36–43, Nov. 2001.

[12] S.-B. Yoon, J. Hur, and D.-S. Hyun, "A method of optimal design of single-sided linear induction motor for transit," *IEEE Trans. Magn.*, vol. 33, no. 5, pp. 4215–4217, Sep. 1997.

[13] M. H. Tosifian and J. Nazarzadeh, "A detailed model of disk type linear induction machines," *Int. Trans. Electr. Energy Syst.*, vol. 25, no. 9, pp. 1736–1747, Sep. 2015.

[14] K. T. Chau, C. C. Chan, and C. Liu, "Overview of permanent-magnet brushless drives for electric and hybrid electric vehicles," *IEEE Trans. Ind. Electron.*, vol. 55, no. 6, pp. 2246–2257, Jun. 2008.

[15] Y. Yasa, M. Elamin, Y. Sozer, J. Kutz, J. S. Tylenda, and R. L. Wright, "Acoustic noise mitigation for high pole count switched reluctance machines through skewing method with multiphysics FEA simulations," *Proc. IEEE Energy Convers. Congr. Expo. (ECCE)*, Oct. 2017, pp. 738–744.

[16] M. Lu and R. Cao, "Comparative investigation of high temperature superconducting linear flux-switching motor and high temperature superconducting linear switched reluctance motor for urban railway transit," *IEEE Trans. Appl. Supercond.*, vol. 31, no. 5, pp. 1–5, Aug. 2021.

[17] R. Cao, W. Huang, and M. Cheng, "A new modular and complementary double-sided linear flux-switching permanent magnet motor with yokeless secondary," in *Proc. 17th Int. Conf. Electr. Mach. Syst. (ICEMS)*, Oct. 2014, pp. 3648–3652.

[18] R. Cao and E. Su, "New double-sided wound field flux-switching linear motor with non-overlapping winding," in *Proc. IEEE Int. Electr. Mach. Drives Conf. (IEMDC)*, May 2019, pp. 1746–1751.

[19] A. Gandhi and L. Parsa, "Hybrid flux-switching linear machine with fault-tolerant capability," *Proc. Int. Electr. Mach. Drives Conf.*, May 2015, pp. 715–720

[20] C. T. Liu, C. C. Hwang, P. L. Li, S. S. Hung, and P. Wendling, "Design optimization of a double-sided hybrid excited linear flux switching PM motor with low force ripple," *IEEE Trans. Magn.*, vol. 50, no. 11, pp. 1–4, Nov. 2014.
[21] W. K. Ullah, S. Faisal, U. Erwan, U. Muhammad, and K. Noman, "Analytical validation of novel consequent pole E-core stator permanent magnet flux switching machine," *IET Electr. Power Appl.*, vol. 14, no. 5, pp. 789–796, 2020.
[22] B. L. J. Gysen, E. Ilhan, K. J. Meessen, J. J. H. Paulides, and E. A. Lomonova, "Modeling of flux switching permanent magnet machines with Fourier analysis," *IEEE Trans. Magn.*, vol. 46, no. 6, pp. 1499–1502, Jun. 2010.
[23] M. G. Munteanu, F. De Bona, and F. Bressan, "Shaft design: A semi-analytical finite element approach," *Mech. Based Des. Struct. Mach.*, vol. 46, no. 2, pp. 184–195, Mar. 2018.
[24] S. R. Aleksandrov, D. C. J. Krop, D. T. E. H. van Casteren, T. T. Overboom, and E. A. Lomonova, "Analytical modelling techniques for thrust force calculation of a permanent magnet linear motor," in *Proc. 11th Int. Symp. Linear Drives Ind. Appl.*, Sep. 2017, pp. 1–6.
[25] Y. Amara and G. Barakat, "Analytical modeling of magnetic field in surface mounted permanent-magnet tubular linear machines," *IEEE Trans. Magn.*, vol. 46, no. 11, pp. 3870–3884, Nov. 2010.
[26] B. Zhang, M. Cheng, R. Cao, Y. Du, and G. Zhang, "Analysis of linear flux-switching permanent magnet motor using response surface methodology," *IEEE Trans. Magn.*, vol. 50, no. 11, pp. 1–4, Nov. 2014.
[27] Y. Laoubi, M. Dhifli, G. Barakat, and Y. Amara, "Hybrid analytical modeling of a flux switching permanent magnet machines," in *Proc. Int. Conf. Elect. Mach. (ICEM)*, Sep. 2014, pp. 1018–1023.
[28] S. Zhou, H. Yu, M. Hu, C. Jiang, and L. Huang, "Nonlinear equivalent magnetic circuit analysis for linear flux-switching permanent magnet machines," *IEEE Trans. Magn.*, vol. 48, no. 2, pp. 883–886, Feb. 2012.
[29] Y. Wang, W. Xu, X. Zhang, and W. Ma, "Harmonic analysis of air gap magnetic field in flux-modulation double-stator electrical-excitation synchronous machine," *IEEE Trans. Ind. Electron.*, vol. 67, no. 7, pp. 5302–5312, Jul. 2020.
[30] B. Gaussens, E. Hoang, O. D. L. Barriere, J. Saint-Michel, M. Lecrivain, and M. Gabsi, "Analytical approach for air-gap modeling of field-excited flux-switching machine: No-load operation," *IEEE Trans. Magn.*, vol. 48, no. 9, pp. 2505–2517, Sep. 2012.
[31] J. Wang, D. Howe, and Z. Lin, "Comparative studies on linear motor topologies for reciprocating vapor compressors," in *Proc. IEEE Int. Electr. Mach. Drives Conf.*, May 2007, pp. 364–369.

NOMAN ULLAH (Member, IEEE) received the B.S. and M.S. degrees in electrical (power) engineering from the University of Engineering and Technology, Peshawar, Pakistan, in 2012 and 2015, respectively, where he is currently pursuing the Ph.D. degree in electrical energy system engineering.

From 2013 to 2015, he was a Research Assistant with the Pakistan Engineering Council. Since 2015, he has been a Lecturer with the Electrical and Computer Engineering Department, COMSATS University Islamabad (Abbottabad Campus), Pakistan. His research interests include design and optimization of linear flux-switching machines and applications.

FAISAL KHAN (Member, IEEE) received the B.S. degree in electronics engineering and the M.S. degree in electrical engineering from COMSATS University Islamabad (Abbottabad Campus), Pakistan, in 2009 and 2012, respectively, and the Ph.D. degree in electrical engineering from Universiti Tun Hussein Onn Malaysia, Malaysia, in 2017.

From 2010 to 2012, he was a Lecturer with the University of Engineering and Technology, Abbottabad, Pakistan. Since 2017, he has been an Assistant Professor with the Electrical and Computer Engineering Department, COMSATS University Islamabad (Abbottabad Campus). He is an author of more than 100 publications, one patent, and received multiple research awards. His research interests include design of flux-switching, synchronous, and dc machines.

ABDUL BASIT received the B.S. degree in electrical engineering from the University of Engineering and Technology, Peshawar, Pakistan, in 2006, the M.S. degree in electrical (power) engineering from the Chalmers University of Technology, Sweden, in 2011, and the Ph.D. degree from the Department of Wind Energy, Technical University of Denmark (DTU), in 2015.

From 2007 to 2009, he was a Field Engineer with NEC Corporation, Pakistan. Since 2015, he has been an Assistant Professor with the Electrical Energy System Engineering Department, Pakistan Center for Advanced Studies in Energy, University of Engineering and Technology. His research interests include modeling and analysis of operation and control of wind generators.

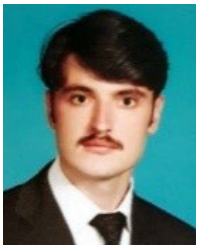

WASIQ ULLAH (Graduate Student Member, IEEE) received the B.S. and M.S. degrees in electrical (power) engineering from the Electrical and Computer Engineering Department, COMSATS University Islamabad (Abbottabad Campus), Pakistan, in 2017 and 2019, respectively, where he is currently pursuing the Ph.D. degree in electrical engineering with the Electrical and Computer Engineering Department.

Since 2017, he has been a Research Assistant with the Electrical and Computer Engineering Department, COMSATS University Islamabad (Abbottabad Campus). His research interests include analytical design and optimization of synchronous and flux-switching machines.

IMRAN HASEEB received the B.S. degree in electrical (power) engineering from the Electrical and Computer Engineering Department, COMSATS University Islamabad (Abbottabad Campus), Pakistan, in 2012, and the M.S. degree in electrical engineering from CECOS University Peshawar, Pakistan, in 2018.

Since 2019, he has been a Lecturer with the Electrical Engineering Department, Qurtuba University, Dera Ismail Khan, Pakistan. His research interest includes analysis of synchronous machines.